



Theoretical investigations on the magneto-Raman effect of CrI₃

Shuang Liu, Meng-Qiu Long, and Yun-Peng Wang ^{*}

School of Physics and Electronics, Hunan Key Laboratory for Super-Microstructure and Ultrafast Process, Central South University, 932 South Lushan Road, Changsha 410083, People's Republic of China

 (Received 4 November 2022; revised 2 July 2023; accepted 2 November 2023; published 16 November 2023)

The magneto-optical property of magnets is used for detecting their magnetization and for information storage applications. The elastic interaction of light with magnetic materials is modulated by the spin-orbital coupling, which is manifested by the rotation of the polarization plane of scattered light with respect to the injected light. The magnetic order also participates in the inelastic Raman scattering of light, as experimentally demonstrated by an $\sim 40^\circ$ rotation of the polarization plane by the two-dimensional ferromagnet CrI₃. In this paper, we investigate the magneto-Raman properties of monolayer CrX₃ ($X = \text{Cl, Br, and I}$) using first-principles methods. We calculate the Raman tensor and the Raman intensity due to the A_{1g} phonon by taking the spin-orbit coupling into account. Experimental results on CrI₃ are well reproduced. Both the rotation angle of the polarization plane of linearly polarized light and the Raman circular polarization strongly depend on the energy of the injected photons.

DOI: [10.1103/PhysRevB.108.184414](https://doi.org/10.1103/PhysRevB.108.184414)

I. INTRODUCTION

Two-dimensional (2D) magnetic materials with layered structures have attracted much attention recently, owing to their diverse physical properties and potential applications [1,2]. The CrI₃ monolayer is the first 2D magnet people have discovered to exhibit spontaneous ferromagnetism [3]. Its Curie temperature is 45 K, and the magnetic easy axis is perpendicular to the atomic plane. The optical properties of these low-dimensional magnetic materials are determined by the couplings among electronic, vibrational, and magnetic degrees of freedom. The emergence of long-range ferromagnetic (FM) order breaks the time-reversal symmetry, resulting in Kerr and Faraday effects. The Kerr effect was used for detecting the spontaneous magnetization of ferromagnetic 2D van der Waals (vdW) materials [3,4]. The time-reversal symmetry breaking induces the difference in the propagating velocities of the left- and right-elliptically polarized light.

It is the ratio between the usually small off-diagonal term and the large diagonal terms of the dielectric tensor that determines the Kerr and Faraday rotation angles. As a result, the polarization of the elastically scattered light rotates with respect to the laser by a small angle on the order of 1° . The magneto-optical Kerr and Faraday properties of CrI₃ and related materials were investigated using first-principles methods based on the independent-particle approximation [5–7] and by including the many-body effects [8].

The Raman effect is another tool for monitoring the magnetic orderings in 2D vdW materials [9,10], which is especially useful for antiferromagnets [11,12]. The Raman effect results from the inelastic scattering of light by quasiparticles in solids such as phonons and magnons. The intensity and polarization of inelastically scattered light are determined

by the change in the optical conductivity tensor due to these quasiparticles, instead of the tensor itself. The rotation of the polarization plane therefore could be much stronger. The magneto-Raman effect of van der Waals magnets was investigated experimentally [13–17]. The inelastically scattered linearly polarized light rotates by about 40° due to the A_g phonon mode in a CrI₃ monolayer [14] and by about 35° due to the A_g phonon mode in a ferromagnetic CrI₃ multilayer [15].

Symmetry analysis of the CrI₃ lattice predicts vanishing off-diagonal elements of the Raman tensor for the nonmagnetic state or when neglecting the spin-orbital coupling effect. For the ferromagnetic state with spin-orbital coupling, there is an antisymmetric term in the Raman tensor, resulting in the finite cross-polarized Raman intensity as well as the rotation of the linearly polarized light. Most previous theoretical work has been focused on the energies and relative intensities of peaks in the Raman shift of CrI₃, which correspond to the phonon modes at the center of the first Brillouin zone with Raman activity [18,19]. The inclusion of the spin-orbital coupling effect is critical for studying the polarized Raman effect [20]. Lei and Coh carried out first-principles calculations on CrI₃ and confirmed the large cross-polarized Raman intensity, in accord with experiments [21].

In this paper, we systematically study the polarized Raman effect of CrX₃ ($X = \text{I, Br, and Cl}$) monolayers using density functional theory (DFT). Our calculations are based on the independent-particle approximation, and the computational details are presented in Sec. II. The calculation results regarding the laser energy dependence of the rotation angle of linear polarization and the circular polarization are discussed in Sec. III, followed by conclusions and perspectives in Sec. IV.

II. COMPUTATIONAL DETAILS

All the calculations were carried out using the projector augmented-wave method within the density functional theory

^{*}yunpengwang@csu.edu.cn

as implemented in the Vienna *ab initio* simulation package (VASP) code [22–26]. Both the local density approximation (LDA) [27] and the Perdew-Burke-Ernzerhof [28] (PBE) parametrization of the generalized gradient approximation of the exchange-correlation functional were used in our calculations. The intra-atomic Coulomb repulsion on the Cr atom was taken into account by using the DFT + U method [29] with the Hubbard U parameter from 0 to 3 eV. The Hubbard correction was routinely added in DFT calculations of CrI₃ and related materials [30–32]. No optimal value of the Hubbard U for CrI₃ and related materials has been proposed in the literature. The spin-orbital coupling effect was considered in the calculations of dielectric tensors by setting “LSORBIT=T” in the INCAR input file for VASP. The lattice constant and the crystal structures of CrX₃ ($X = \text{I, Br, and Cl}$) monolayers were optimized until the atomic forces were less than 0.001 eV/Å. An 11×11 k mesh was used for structural optimization. The cutoff energy of the plane-wave basis is set to 500 eV.

The dielectric tensor at different energies was calculated under the independent-particle approximation [33]. The excitonic and local-field effects are ignored. The excitonic effects are important for the magneto-optical properties of CrI₃ and related materials [8,34]. In this paper we neglected the excitonic effect to reduce the computational cost. Our benchmark calculations show that a uniform 15×15 k mesh and a total number of 200 bands are sufficient to converge the dielectric tensor between 1 and 5 eV; this setting was used in all the dielectric tensor calculations.

The frequencies and eigenvectors of phonon modes at the center of the Brillouin zone were calculated using the density functional perturbation theory as implemented in the VASP code. The electric polarization vectors of both the incident and scattered light (\vec{e}_L and \vec{e}_S , respectively) are within the monolayer atomic plane in the backscattering geometry. The Raman intensity $I(E)$ is given by the Raman tensor \mathbf{R}^μ corresponding to a phonon mode μ :

$$I^\mu(E) \propto |(\vec{e}_L)^T \cdot \mathbf{R}^\mu(E) \cdot \vec{e}_S|^2, \quad (1)$$

where E is the photon energy of the laser. The Raman tensor \mathbf{R}^μ is the changes in the dielectric tensor $\epsilon(E)$ induced by phonon mode μ :

$$\mathbf{R}^\mu(E) = \frac{\partial \epsilon(E)}{\partial u^\mu}, \quad (2)$$

where u^μ represents the amplitude of phonon mode μ . In this paper we will only consider the Raman effect due to one phonon mode; thus the superscript μ is then dropped.

III. RESULTS

We first calculate the phonon modes at the center of the first Brillouin zone, whose frequencies correspond to the Raman shift. The calculated phonon frequencies using different flavors of the exchange-correlation functional, including the LDA + U and the PBE + U with the value of the Hubbard U being from 0 to 3 eV, are fairly consistent with each other and with the experimental data; see Table I. The frequencies of the two A_{1g} modes are 75 and 120 cm⁻¹, in good agreement with

TABLE I. The calculated frequencies in units of cm⁻¹ of monolayer CrI₃ for selected phonon modes at the center of the first Brillouin zone. The calculated band gaps in units of eV are listed in the last column.

Symmetry	E_g	A_{1g}	A_{1g}	Band gap
LDA + U				
$U = 0$ eV	237.7	129.5	69.8	1.22
$U = 1$ eV	239.1	127.8	69.7	1.33
$U = 2$ eV	239.9	125.9	69.9	1.29
$U = 3$ eV	240.0	123.7	69.6	1.21
PBE + U				
$U = 0$ eV	225.3	120.7	72.7	1.25
$U = 1$ eV	226.8	119.2	73.3	1.20
$U = 2$ eV	226.5	117.0	72.8	1.11
$U = 3$ eV	225.7	115.0	71.6	1.01
Expt.	237	127.4, 128, 129	76.7, 79	1.30

previous experimental and theoretical results [18,19,35]. The LDA + U method reproduces the experimental Raman shift slightly better than the PBE + U approach. The calculated phonon frequencies exhibit only a slight dependence on the value of the Hubbard U . This is because the occupations of Cr- d orbitals persist (t_{2g} orbitals in one spin channel are occupied, while all other Cr- d orbitals remain unoccupied) and the electronic structure remains insulating as the value of the Hubbard U increases. In this paper we are particularly interested in the A_{1g} mode with a frequency of about 128 cm⁻¹. This mode only involves the out-of-phase and out-of-plane motions of the I atoms. In addition, the calculated band gap of the CrI₃ monolayer is also listed in the last column of Table I. The calculated band gap ranges from 1.0 to 1.3 eV, in fairly good agreement with theoretical and experimental results [36,37]. The band gap has a weak dependence on the Hubbard U parameter, because CrI₃ is a charge-transfer insulator instead of a Mott insulator.

We turn to the simulations of the polarized Raman effect due to the A_{1g} phonon mode. In accord with the experimental setup, we consider that both the laser and the scattered light propagate vertically with respect to the atomic plane. Therefore the third component of the polarization vectors \vec{e}_L and \vec{e}_S in Eq. (1) is equal to zero. The Raman intensity is thus only determined by the xx , yy , xy , and yx components of the Raman tensor \mathbf{R} . Equivalently, one can take the polarization vectors \vec{e}_L and \vec{e}_S with two components, and the Raman tensor \mathbf{R} is reduced to a 2×2 tensor.

We firstly consider that the laser is linearly polarized. The angle between the polarization plane and the lattice vector \mathbf{a} of the CrI₃ monolayer is denoted as θ_L . The scattered Raman light passes through a linear analyzer. The angle between the polarization vector of the analyzer and the lattice vector \mathbf{a} is denoted as θ_S . The polarization vectors as defined in Eq. (1) are $\mathbf{e}_L = (\cos \theta_L, \sin \theta_L)$ and $\mathbf{e}_S = (\cos \theta_S, \sin \theta_S)$. We calculate the Raman intensity using Eq. (1) as a function of θ_L and θ_S . The magnetic moments of Cr ions point to the + z direction, perpendicular to the atomic plane. The photon energy is set to $E = 2$ eV corresponding to the 632-nm laser used in experiments.

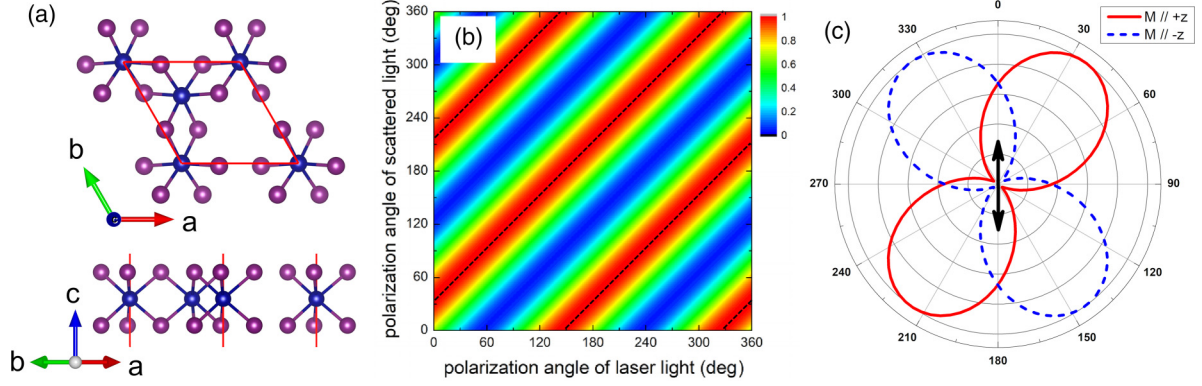


FIG. 1. (a) Top and side views of the CrI_3 monolayer; the red lines stand for the edges of the primitive cell. (b) The calculated Raman intensity of monolayer CrI_3 as a function of the polarization angles of the laser and the scattered Raman light. The dashed lines are a guide for the eye for the maxima of the Raman intensity. (c) Polar plot of the calculated Raman intensity vs the polarization angle of the scattered Raman light for magnetization along the $+z$ and $-z$ directions; the double-headed arrow denotes the polarization of the laser. All the angles are measured from the lattice vector \mathbf{a} . Calculations are performed using LDA + U with $U = 2$ eV.

The Raman intensity calculated using the LDA + U functional with $U = 2$ eV, normalized by the maximum value, is shown as pseudocolor in Fig. 1(b). The Raman intensity is only a function of the difference between θ_L and θ_S ; the same is observed in all calculations using LDA + U and PBE + U .

The dependence of the Raman intensity on the angle difference ($\theta_L - \theta_S$) can also be deduced from analysis of the symmetry. The Raman tensor of the A_{1g} phonon mode of the CrI_3 monolayer has the form

$$\mathbf{R} = \begin{pmatrix} a & b \\ -b & a \end{pmatrix}, \quad (3)$$

where both a and b are generally complex numbers [21], which was confirmed by our DFT calculations. The Raman intensity can be calculated as

$$I \propto \left| \begin{pmatrix} \cos \theta_S & \sin \theta_S \\ \sin \theta_S & \cos \theta_S \end{pmatrix} \cdot \begin{pmatrix} a & b \\ -b & a \end{pmatrix} \cdot \begin{pmatrix} \cos \theta_L \\ \sin \theta_L \end{pmatrix} \right|^2 \quad (4)$$

$$= |a \cos(\theta_S - \theta_L) - b \sin(\theta_S - \theta_L)|^2 \quad (5)$$

indicating that the Raman intensity is only a function of $\theta_L - \theta_S$, which is consistent with our calculation results shown in Fig. 1.

Taking $\theta_L = 0^\circ$, the calculated Raman intensity as a function of θ_S is plotted as the red curve in Fig. 1(c). The maximum of the Raman intensity occurs at $\theta_S = 38.7^\circ$, indicating that the polarization of Raman scattered light is rotated by this angle with respect to the laser light. Hereinafter we denote this angle as the rotation angle. The calculated value of the rotation angle agrees well with the experimental values [14,15].

We do the same calculation with the magnetic moments of Cr ions along the $-z$ direction ($\mathbf{M} \parallel -z$). The calculated Raman intensity is again only dependent on the angle difference $\theta_L - \theta_S$. Setting $\theta_L = 0$, the calculated Raman intensity as a function of θ_S is shown as the dashed blue curve in Fig. 1(c). The polarization rotation angle is -38.7° , whose absolute value agrees with the $\mathbf{M} \parallel +z$ case but with an opposite sign. This result is also consistent with experiments [14].

As mentioned in the Introduction, the spin-orbit coupling is critical for understanding the polarized Raman properties. To prove this, the above calculations are also performed without including the spin-orbit coupling effect. In this case, the maxima of Raman intensity occur at $\theta_L = \theta_S$, that is, where the rotation angle of the polarized Raman light is equal to zero. So the spin-orbit coupling (SOC) is an essential component of the theory for the polarized Raman effect. The effect of SOC can be understood by analyzing the crystal symmetry [21]. The space group of CrI_3 is $R\bar{3}1'$ if one does not consider the spin-orbital coupling. In this case, the off-diagonal element b of the Raman tensor diminishes. Once the spin-orbital coupling is considered, the space group is reduced to $R\bar{3}$, and the off-diagonal element b is allowed to be nonzero.

We note that the precise value of the rotation angle of the polarized Raman light depends on the flavor of the exchange-correlation functional and the value of the Hubbard U used in the calculations. The rotation angles corresponding to a laser energy of 2.0 eV are listed in Table II by using both LDA + U and PBE + U with different choices of the U parameter. When the value of U is set to zero, that is, no intra-atomic Coulomb repulsion is included, the rotation angle is severely underestimated. The inclusion of U cures the problem and predicts a rotation angle between 33° and 48° , qualitatively reproducing the experimental results. The agreement with experiments indicates the importance of intra-atomic Coulomb repulsion for description of the interaction with light.

TABLE II. The calculated rotation angle between the polarization directions of the laser and the scattering light ($|\theta_S - \theta_L|$) in units of degrees and the Raman circular polarization ρ (see the text for its definition) given as a percentage. The photon energy is set to 2.0 eV. The experimental data are taken from Ref. [14].

Functional	LDA + U			PBE + U			Expt.		
	0	1	2	0	1	2			
U (eV)	0	1	2	0	1	2	—		
$ \theta_S - \theta_L $ (deg)	15.0	33.5	38.7	35.2	12.7	35.7	42.2	47.9	~40
ρ (%)	79	35	46	29	12	36	12	33	~60

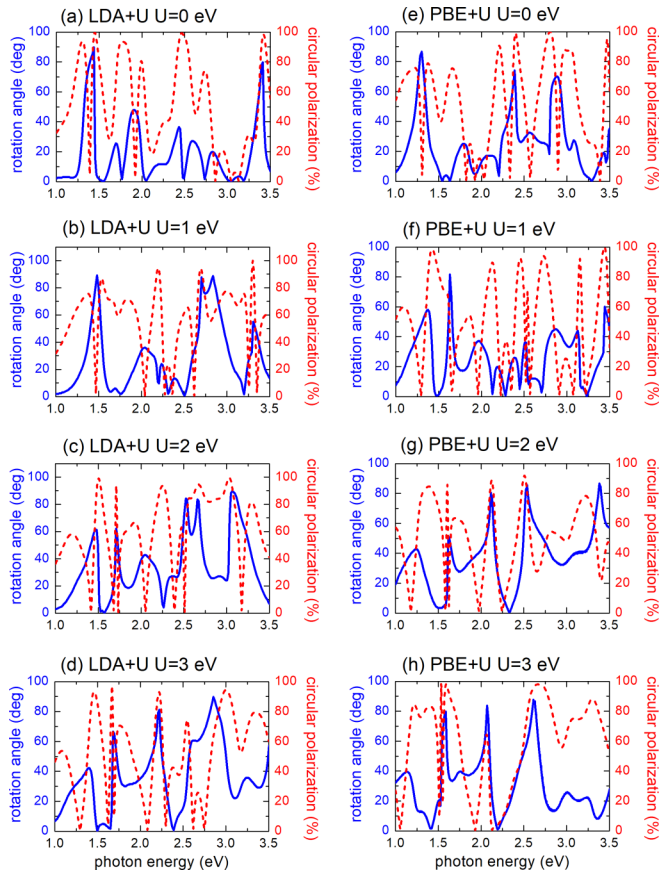


FIG. 2. The calculated rotation angle of linearly polarized Raman light (blue solid curves) and the calculated Raman circular polarization (red dashed curves). The results are calculated using the LDA + U functional with (a) $U = 0$ eV, (b) $U = 1$ eV, (c) $U = 2$ eV, and (d) $U = 3$ eV and using the PBE + U functional with (e) $U = 0$ eV, (f) $U = 1$ eV, (g) $U = 2$ eV, and (h) $U = 3$ eV.

The photon energy, serving as a parameter in our calculations of the dielectric tensor and the Raman tensor, corresponds to different laser sources used in experiments. As a function of the laser photon energy, the rotation angles calculated using LDA + U and PBE + U functionals with different choices of Hubbard U parameters are plotted in Fig. 2. In all the cases, the calculated rotation angle strongly oscillates as a function of the laser photon energy. As the Hubbard U increases from 0 to 3 eV, the features in the calculated-rotation-angle curve evolve in a rather complicated way. For the LDA + U results, a peak slightly below 1.5 eV persists, but a new peak emerges at 1.7 eV for $U = 2$ eV and $U = 3$ eV; both the case of $U = 1$ eV and the case of $U = 2$ eV show a broad peak around 2.0 eV which, however, vanishes and becomes a dip for the case of $U = 3$ eV. The LDA + U with $U = 3$ eV result has a similar shape to the PBE + U results with $U = 2$ eV and $U = 3$ eV: The rotation angle is predicted to reach $\sim 90^\circ$ at photon energies of around 1.7 eV and around 2.1 eV. These predictions can be tested by experiments using different laser sources.

The reason underlying the large polarization rotation is analyzed by tracing the modulation of the electronic band structure and the dielectric tensor due to the A_{1g} phonon

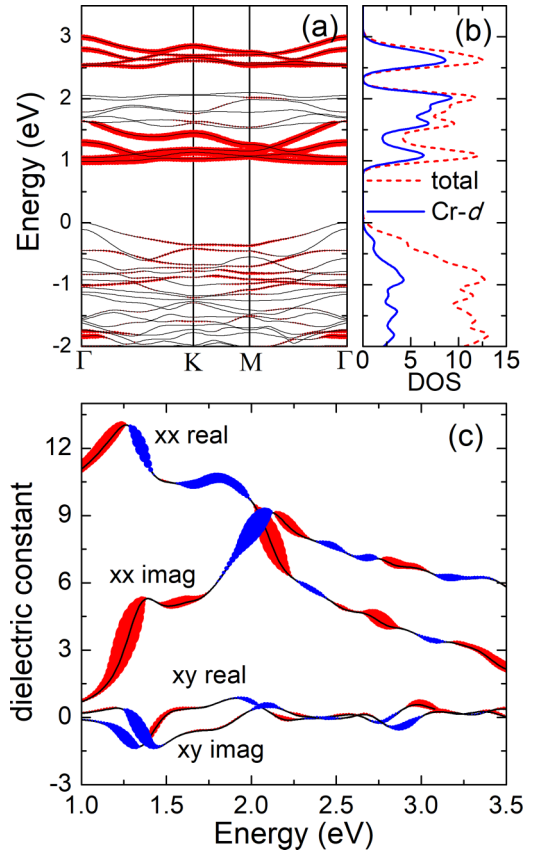


FIG. 3. Effects of the A_{1g} phonon mode on the electronic structure and dielectric tensor of CrI_3 monolayer using the LDA + U with $U = 1$ eV. (a) The calculated electronic band structure; the size of the red dots stands for the increments of band energies due to the A_{1g} phonon mode. (b) The calculated total density of states (the red dashed curve) and the density of states (DOS) projected on Cr- d orbitals (the blue solid curve). (c) The deviations in the real and imaginary (imag) parts of the xx and xy components of the dielectric tensor due to the A_{1g} phonon mode; the positive and negative deviations are represented by red and blue dots, respectively, and the size of the dots stands for the amplitude of the deviations. The I atoms are moved by 0.3 \AA to produce the results in (a) and (c).

mode. Figure 3(a) shows the modulation of the band structure, where the size of the symbols represents increments of band energies. The projected density of states shown in Fig. 3(b) indicates that the A_{1g} phonon mode modulates the Cr- d -dominated bands in a rigid way. The lowest conduction bands near 1 eV exhibit significant susceptibility to the A_{1g} phonon mode. Besides these bands, the next-higher-energy bands showing significant susceptibility appear above 2.5 eV and are also dominated by the Cr- d orbitals; see Fig. 3(a). Therefore, judging from the energy difference between the valence and conducting bands, one can deduce that the lowest conduction bands near 1 eV serve as the final states of electronic transitions responsible for the peaks at 1.5, 2.0, and 2.7 eV in the curve of rotation angle as shown in Fig. 2(b). One can also see from Fig. 3(c) that at these energies, all the components of the dielectric tensors indeed show large susceptibility to the A_{1g} phonon mode.

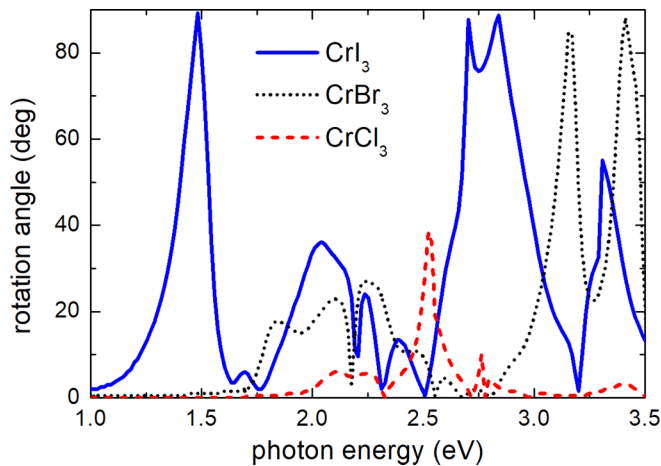


FIG. 4. Comparison between CrI_3 , CrBr_3 , and CrCl_3 . The rotation angles of linearly polarized Raman light are calculated using the LDA + U functional with $U = 1$ eV for CrI_3 (blue solid curve), CrBr_3 (black dotted curve), and CrCl_3 (red dashed curve).

We also consider the case of a circularly polarized laser. The polarization vectors of a circularly polarized light can be expressed by the Jones vectors of $\mathbf{e}_l = (1, i)/\sqrt{2}$ for left-hand circularly polarized light and $\mathbf{e}_r = (1, -i)/\sqrt{2}$ for right-hand circularly polarized light. For the left-to-left (right-to-right) channel, both the vector \mathbf{e}_L and the vector \mathbf{e}_S in Eq. (1) are set to \mathbf{e}_l (\mathbf{e}_r), and the $(\mathbf{e}_S)^T$ in Eq. (1) is interpreted as the complex conjugate transpose. Our calculations confirm that the Raman intensity is exactly zero in both the left-to-right and the right-to-left channels. The calculated Raman intensities in the left-to-left and right-to-right channels are nonzero, but they are different. We compute the Raman circular polarization, defined as $\rho = |\text{LL} - \text{RR}|/(\text{LL} + \text{RR})$, where LL and RR stand for the Raman intensity in the left-to-left and the right-to-right channels. The calculated ρ at photon energy of 2.0 eV is given in Table II. Except for the LDA + U with $U = 0$ eV, other calculations give a smaller ρ than the experimental data. The calculated ρ at different photon energies, shown in Fig. 2 by the dashed curves, are characterized by peaks around 2.2 eV and around 1.8 eV. This may explain the large scattering in the data of ρ shown in Table II.

Finally, we consider other materials in the same group including CrBr_3 and CrCl_3 . They have the same atomic structure as CrI_3 , but the lighter anion leads to weaker spin-orbital coupling strength. Our calculations show that they possess the same band-gap breathing A_{1g} phonon mode as CrI_3 , because they have the same atomic structure. LDA + U with $U = 1$ eV predicts that the A_{1g} mode is at 180.4 cm^{-1} for CrBr_3 and 295.8 cm^{-1} for CrCl_3 . The relatively higher frequency of A_{1g} modes is due to the smaller atomic masses of Br and Cl. The relative rotation angle of linear polarization at a photon energy of 2.0 eV is 17° for CrBr_3 , while it is only 2° for CrCl_3 . Here we consider the out-of-plane magnetization configuration of CrCl_3 for a direct comparison. As discussed for CrI_3 , the polarization rotation angle has a strong dependence on the photon energy. In Fig. 4 we compare the photon energy dependence of polarization rotation angles of CrX_3 ($X = \text{Cl}$, Br, and I). Around 2 eV, the rotation angle of CrBr_3 is within roughly the same range as for CrI_3 , but the rotation angle of CrCl_3 is much smaller within the whole energy range. These materials have quite similar atomic, magnetic, and phononic properties, and the only difference is the spin-orbit coupling strength of anions. Judged from the polarization rotation angle, we confirm that Cl has the weakest spin-orbital coupling as expected; however, I and Br are comparable.

IV. CONCLUSION

We have studied the magneto-Raman properties of 2D ferromagnetic semiconductors CrX_3 ($X = \text{Cl}$, Br, and I). The rotation angle of the polarization plane of linearly polarized light and the Raman circular polarization show strong dependence on the photon energy as well as on the exchange-correlation functional. The excitonic effects on the magneto-Raman properties will be investigated in future work.

ACKNOWLEDGMENTS

This work is supported by the National Natural Science Foundation of China (Grant No. 12004439) and computational resources from the High Performance Computing Center of Central South University.

- [1] K. S. Burch, D. Mandrus, and J.-G. Park, *Nature (London)* **563**, 47 (2018).
- [2] C. Gong and X. Zhang, *Science* **363**, eaav4450 (2019).
- [3] B. Huang, G. Clark, E. Navarro-Moratalla, D. R. Klein, R. Cheng, K. L. Seyler, D. Zhong, E. Schmidgall, M. A. McGuire, D. H. Cobden, W. Yao, D. Xiao, P. Jarillo-Herrero, and X. Xu, *Nature (London)* **546**, 270 (2017).
- [4] C. Gong, L. Li, Z. Li, H. Ji, A. Stern, Y. Xia, T. Cao, W. Bao, C. Wang, Y. Wang, Z. Q. Qiu, R. J. Cava, S. G. Louie, J. Xia, and X. Zhang, *Nature (London)* **546**, 265 (2017).
- [5] G. Guo, G. Bi, C. Cai, and H. Wu, *J. Phys.: Condens. Matter* **30**, 285303 (2018).
- [6] V. K. Gudelli and G.-Y. Guo, *New J. Phys.* **21**, 053012 (2019).
- [7] K. Yang, W. Hu, H. Wu, M.-H. Whangbo, P. G. Radaelli, and A. Stroppa, *ACS Appl. Electron. Mater.* **2**, 1373 (2020).
- [8] M. Wu, Z. Li, T. Cao, and S. G. Louie, *Nat. Commun.* **10**, 2371 (2019).
- [9] K. Kim, J.-U. Lee, and H. Cheong, *Nanotechnology* **30**, 452001 (2019).
- [10] Y.-J. Sun, S.-M. Pang, and J. Zhang, *Chin. Phys. B* **30**, 117104 (2021).
- [11] J.-U. Lee, S. Lee, J. H. Ryoo, S. Kang, T. Y. Kim, P. Kim, C.-H. Park, J.-G. Park, and H. Cheong, *Nano Lett.* **16**, 7433 (2016).
- [12] K. Kim, S. Y. Lim, J.-U. Lee, S. Lee, T. Y. Kim, K. Park, G. S. Jeon, C.-H. Park, J.-G. Park, and H. Cheong, *Nat. Commun.* **10**, 345 (2019).
- [13] Y. Zhang, X. Wu, B. Lyu, M. Wu, S. Zhao, J. Chen, M. Jia, C. Zhang, L. Wang, X. Wang, Y. Chen, J. Mei, T. Taniguchi, K. Watanabe, H. Yan, Q. Liu, L. Huang, Y. Zhao, and M. Huang, *Nano Lett.* **20**, 729 (2020).

- [14] B. Huang, J. Cenker, X. Zhang, E. L. Ray, T. Song, T. Taniguchi, K. Watanabe, M. A. McGuire, D. Xiao, and X. Xu, *Nat. Nanotechnol.* **15**, 212 (2020).
- [15] A. McCreary, T. T. Mai, F. G. Utermohlen, J. R. Simpson, K. F. Garrity, X. Feng, D. Shcherbakov, Y. Zhu, J. Hu, D. Weber, K. Watanabe, T. Taniguchi, J. E. Goldberger, Z. Mao, C. N. Lau, Y. Lu, N. Trivedi, R. Valdés Aguilar, and A. R. Hight Walker, *Nat. Commun.* **11**, 3879 (2020).
- [16] B. Lyu, Y. Gao, Y. Zhang, L. Wang, X. Wu, Y. Chen, J. Zhang, G. Li, Q. Huang, N. Zhang, Y. Chen, J. Mei, H. Yan, Y. Zhao, L. Huang, and M. Huang, *Nano Lett.* **20**, 6024 (2020).
- [17] W. Jin, Z. Ye, X. Luo, B. Yang, G. Ye, F. Yin, H. H. Kim, L. Rojas, S. Tian, Y. Fu, S. Yan, H. Lei, K. Sun, A. W. Tsen, R. He, and L. Zhao, *Proc. Natl. Acad. Sci. USA* **117**, 24664 (2020).
- [18] D. T. Larson and E. Kaxiras, *Phys. Rev. B* **98**, 085406 (2018).
- [19] L. Webster, L. Liang, and J.-A. Yan, *Phys. Chem. Chem. Phys.* **20**, 23546 (2018).
- [20] J. Kuneš, *Phys. Scr.* **T109**, 116 (2004).
- [21] M. Lei and S. Coh, *Phys. Rev. Mater.* **5**, 025202 (2021).
- [22] G. Kresse and J. Hafner, *Phys. Rev. B* **47**, 558 (1993).
- [23] G. Kresse and J. Hafner, *Phys. Rev. B* **49**, 14251 (1994).
- [24] G. Kresse and J. Furthmüller, *Comput. Mater. Sci.* **6**, 15 (1996).
- [25] G. Kresse and J. Furthmüller, *Phys. Rev. B* **54**, 11169 (1996).
- [26] G. Kresse and D. Joubert, *Phys. Rev. B* **59**, 1758 (1999).
- [27] J. P. Perdew and A. Zunger, *Phys. Rev. B* **23**, 5048 (1981).
- [28] J. P. Perdew, K. Burke, and M. Ernzerhof, *Phys. Rev. Lett.* **77**, 3865 (1996).
- [29] S. L. Dudarev, G. A. Botton, S. Y. Savrasov, C. J. Humphreys, and A. P. Sutton, *Phys. Rev. B* **57**, 1505 (1998).
- [30] N. Sivadas, S. Okamoto, X. Xu, C. J. Fennie, and D. Xiao, *Nano Lett.* **18**, 7658 (2018).
- [31] F. Xue, Y. Hou, Z. Wang, and R. Wu, *Phys. Rev. B* **100**, 224429 (2019).
- [32] P. Jiang, C. Wang, D. Chen, Z. Zhong, Z. Yuan, Z.-Y. Lu, and W. Ji, *Phys. Rev. B* **99**, 144401 (2019).
- [33] M. Gajdoš, K. Hummer, G. Kresse, J. Furthmüller, and F. Bechstedt, *Phys. Rev. B* **73**, 045112 (2006).
- [34] A. Molina-Sánchez, G. Catarina, D. Sangalli, and J. Fernández-Rossier, *J. Mater. Chem. C* **8**, 8856 (2020).
- [35] W. Jin, H. H. Kim, Z. Ye, S. Li, P. Rezaie, F. Diaz, S. Siddiq, E. Wauer, B. Yang, C. Li, S. Tian, K. Sun, H. Lei, A. W. Tsen, L. Zhao, and R. He, *Nat. Commun.* **9**, 5122 (2018).
- [36] W.-B. Zhang, Q. Qu, P. Zhua, and C.-H. Lam, *J. Mater. Chem. C* **3**, 12457 (2015).
- [37] L. Tomarchio, S. Macis, L. Mosesso, L. T. Nguyen, A. Grilli, M. C. Guidi, R. J. Cava, and S. Lupi, *Sci. Rep.* **11**, 23405 (2021).